Proceedings of the 2018 IEEE
International Conference on Robotics and Biomimetics
December 12-15, 2018, Kuala Lumpur, Malaysia

Real-time Dynamic Models for Soft Bending Actuators

Isuru S. Godage*, Yue Chen†, Kevin C. Galloway‡, Emily Templeton#, Brian Rife#, and Ian D. Walker§

***Abstract*—Soft robotics has witnessed increased attention from the robotic community due to their desirable features in compliant manipulation in unstructured spaces and human-friendly applications. Their light-weight designs and low-stiffness are ideally suited for environments with fragile and sensitive objects without causing damage. Deformation sensing of soft robots so far has relied on highly nonlinear bending sensors and vision-based methods that are not suitable for obtaining precise and reliable state feedback. In this work, for the first time, we explore the use of a state-of-the-art high fidelity deformation sensor that is based on optical frequency domain reflectometry in soft bending actuators. These sensors are capable of providing spatial coordinate feedback along the length of the sensor at every 0.8 mm at up to 250 Hz. This work systematically analyzes the sensor feedback for soft bending actuator deformation and then introduces a reduced order kinematic model, together with cubic spline interpolation, which could be used to reconstruct the continuous deformation of the soft bending actuators. The kinematic model is then extended to derive an efficient dynamic model which runs at 1.5 kHz and validated against the experimental data.**

I. Introduction

The advancement of bio-inspired soft robots, featuring high compliance and inherent safety of operation, in contrast to traditional rigid-bodied, precise but often dangerous robots, opens up novel research paradigms. Soft robotics is an umbrella term that herein is used to cover all types of active and physically reactive compliant systems where the term "soft" is used in different contexts: from completely soft deformable robots to the compliant joints in serial rigid linked robots. In this paper, we particularly focus on soft bending actuators (SBA) that can bend, twist, and/or elongate, actively or passively, during operation.

Soft robots, in the sense of "completely" deformable robot systems, has been a highly active area of research in the past few years [1], [2], [3], [4]. Soft robots in this sense have often been made of soft materials such as elastomeric polymers, allowing them to continuously change their shape with a few degrees of freedom (DOF) to form "organic" shapes (in contrast to fixed "geometric shapes" of rigid-bodied robots). An impressive number of prototypes have been proposed to date which employ a range of actuation methods including compressed fluids (e.g. pneumatic and hydraulics), shape memory alloys, electroactive polymers, and magnetic fluids [5], [6]. Because of the passive deformation these robots undergo, during operation and in the face of external forces, they are considered as infinite DOF systems and therefore highly underactuated. By appropriately arranging these SBAs, one can generate complex behaviors aimed at a wide spectrum of motion types including manipulation, whole arm grasping, snake locomotion, legged locomotion [7], [8], peristaltic locomotion, adaptive soft grippers [9], surgical robots, and rehabilitation robots [10].

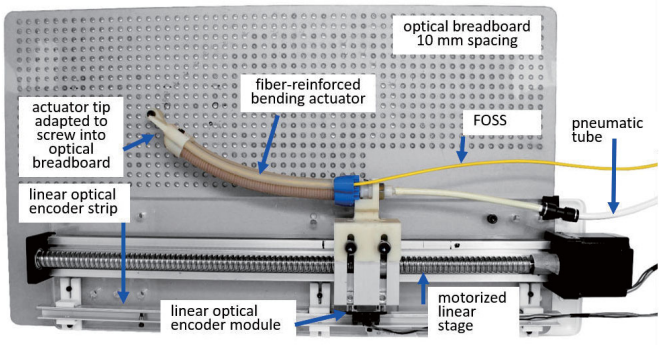

Fig. 1. Soft bending actuator (SBA) experimental setup.

To date, much of the work has focused on open-loop control methods where the desired actuation patterns are pre-programmed [11]. This approach could demonstrate the overall potential yet fails to adapt to environmental changes. Despite an impressive amount of research in SBA that established the immense potential [12], they are yet to make their mark outside laboratory settings. This is due in part to the lack of sophisticated dynamic models that can be used in real-time and complimentary sensing solutions capable of providing accurate, real-time shape deformation data. In this paper, the term real-time is used to indicate the running times faster or equal to actual time. While some modeling approaches have been presented ([13], [14]), most of the modeling approaches that have been presented involves systematic derivation of the statics based on the mechanical properties of SBA. Though rigorous, the approach presents challenges for applications in dynamic control such as static models, where deformation is defined as a function of pressure and only captures the steady state shape deformation. In reality, fluidic actuators are known for their high hysteretic behavior during dynamic motion [15]. Consequently, the static models provide limited

* School of Computing, DePaul University, Chicago, IL 60604. email: igodage@depaul.edu.† Dept. of Mechanical Engineering, University of Arkansas, Fayetteville, AR 72701. ‡ Dept. of Mechanical Engineering, Vanderbilt University, Nashville, TN 37212, # Luna Innovations Inc., Blacksburg, VA. § Dept. of Electrical and Computer Engineering, Clemson University, SC 29634.

This work is supported in part by the National Science Foundation grant IIS-1718755.

978-1-7281-0377-8/18/$31.00 © 2018 IEEE

use in fast applications where hysteresis dominates the overall shape deformation.

Unfortunately, the sensing techniques employed in soft robot control have been inadequate to exploit the advantages of soft robots. For example, image based sensing has been the highest fidelity feedback method capable of measuring the entire shape deformation in real-time: however this requires special background requirements to assist the image high speed processing and thus limits the robot's application space. In addition, occlusions (or line-of-sight) present a significant obstacle, particularly, when the robots are expected to deform significantly. Other sensing methods include bending sensors and strain sensors. The most common approach is to measure the tip coordinates. However, tip information is not a good measure of the entire soft robot shape as it could be in any one state out of infinitely many possibilities due to the high compliance (similar to inverse kinematics of redundant systems [16], [17]). Thus, tip measurements are of limited value as a sufficient feedback method for SBA control. In this respect, fiber optic shape sensors (FOSS) could serve as high-fidelity position sensors for soft robots.

In this study, we integrated a high resolution FOSS into a soft, fiber-reinforced, bending actuator to obtain precise position data at 0.8 mm intervals along the length of the sensor at 75 Hz. This level of high density data has not previously been applied in soft robotic research and thus opens up new research avenues on how such shape data may be used to enable applications previously deemed infeasible for soft robots. In addition to introducing the FOSS in soft robotics, our objective in this paper is to introduce a reduced-order dynamic model for SBA without betraying the overall bending deformation. The motivation for the proposed approach stems from the need to derive a sufficiently sophisticated model that could benefit from the high density data at the same time producing real-time dynamic modeling results.

This paper is arranged as follows. In Section II we first briefly introduce the FOSS system and the integration thereof to a fiber-reinforced SBA. Section III systematically develops the complexity of the reduced order kinematic model to have minimal deformation shape deviation from the experimental results. We then derive the dynamic model for the bending actuator and show that the dynamic model simulates highly dynamic motion with a high degree of overall accuracy. Concluding remarks and future work follow in Section V.

II. Experimental Setup

An overview of the test bed is presented in Fig. 1, where a Matlab Simulink Realtime operated digital valve was used to pressurize the actuator at desired pressure levels while a pressure sensor recorded the pressure readings. The SBA was fabricated in-house by using a multi-step manufacturing method reported in [18] for molding elastomeric tubular bladders with fiber reinforcements (Fig. (2)). SBA bending portion is semi-annular in cross section and 17 cm long and weighs 69 g. The fiber-reinforced wall thickness, w, is estimated to be $4\,mm$ with $r_1 = 14\,mm$ and $r_2 = 10\,mm$. The fibers

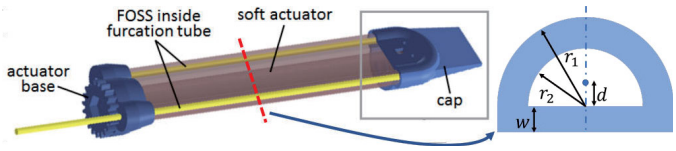

Fig. 2. (Left) Integration of fiber optic shape sensor (FOSS) into the soft bending actuator, and (Right) the cross-section of the SBA.

constrain the radial strain to generate bending deformation and increase the operating pressure range and the resulting output force. During the molding process, Teflon lined lumens were co-molded into the body of the actuator along the edges of the strain limiting layer (i.e. neutral axis). The lumens served a structural purpose to hold the FOSS in position without significantly altering the active free deflection range of motion of the actuator (see Fig. 2). The FOSS sensor comes housed in a 3 mm outside diameter furcation tube (Fiber Instrument Sales, Inc., Oriskany, NY, part #: F00FR3NUY) that is intended to restrain the sensor from bending beyond its 10 mm radius of curvature and provide a low friction housing for the FOSS to slide in to prevent the FOSS from experiencing potentially damaging compressive and tensile loads during handling. Consequently, it presents a challenge to find the end points of the sensor that marks the tip of the SBA. To overcome this problem, we included a cap at the tip of the actuator with a known and constant curvature [19]. Thus, from experimental data, we could identify the point where the Z-directional gradient reaches the maximum value, as the tip point. Having the robot tip position, the soft robot segment within the cap can be derived from the soft robot and cap dimension. The complete SBA with the FOSS sensor was then rigidly attached to the table, in the FOSS's XY plane, for gathering the dynamic data.

In this pilot study, we use an experimental FOSS from Luna Innovations Inc, Blacksburg, VA. The operating principle underlying this FOSS platform is based on Optical Frequency Domain Reflectometry (OFDR) [20]. A more detailed discussion of the optics and mathematics that are used to make these high definition, high sensitivity OFDR measurements can be found in [21]. There are several features worth noting about the FOSS platform. The fiber optic cable is compliant with an ending radius of curvature as low as 10 mm, and can maintain functionality under significant morphological variation. FOSS can detect bending and twisting along the entire length of the sensor with sensor measurements every 0.8 mm, thus enabling high fidelity full 3D state estimation with sampling rates up to 250 Hz. Furthermore, FOSS can be integrated into soft material robotic structures thus eliminating the need for line of sight, especially within non-engineered and fluidic environments.

III. System Model

A. Reduced-Order Model

FOSS-based continuous sensing along a SBA provides a close-up look at the system state and enables investigation

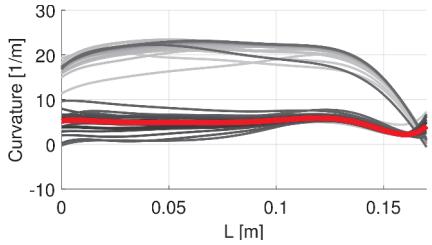

Fig. 3. Curvature variation along the length of the SBA during a 240 kPa step input. Notice the significant curvature fluctuation which give rise to the need for new models to account for such variation.

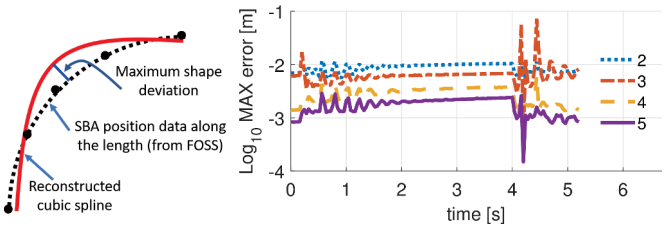

(a) (b)

Fig. 4. Comparing the maximum deformation shape departure for several reduced order, discrete approximations. (a) Measuring the maximum shape deformation of the cubic spline curve reconstruction from discrete position coordinates, (b) Maximum error comparison for 2-5 point approximation. The 5-link system showed a good balance between accuracy (0.0024 m maximum error and 0.0012 m mean error) for the duration of the experiment.

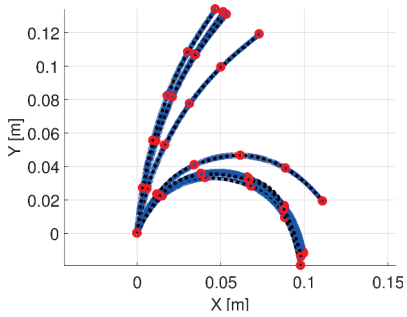

Fig. 5. Comparison of the measured versus the reconstructed shape deformation for a few instances of the SBA deformation during an experiment using 240 kPa step response (Fig. 4). + marks denote the experimental data, o marks identify the joint coordinates of the reduced-order model, and the solid line shows the cubic spline interpolation. Notice the negligible shape difference.

into the limitations of current models. For instance, almost all SBA models to-date, assume uniform material distribution and thus by the resulting models bend in uniform circular arc shapes (constant curvature along the arm). But due to the SBA fabrication process, slight variations in physical parameters (material thickness and density along the length) are common. As a result, the curvature of the actuator, even when it is not actuated, is non-circular. Fig. 3 shows the initial curvature variation (red color line) along the SBA. The figure also shows how the the curvature profile is not maintained and undergoes significant change during actuation. Hence, new models that could account for such nonlinearities need to be proposed.

Ideally, a high-DOF discrete jointed system would be used to represent the nonlinear deformation. But, similar to finite element models, such models suffer from numerical efficiency demands of real-time applications. Hence we propose to combine a low-order approximation together with cubic spline interpolation to reconstruct the continuous deformation. To determine the lowest order with acceptable shape reconstruction capability, we used experimental data collected from the SBA for a step response. The data provides the spatial Cartesian (XYZ) trajectories for points along the entire length of the 17 cm SBA at 0.8 mm apart. At any time instance, there are 212 such points denoting the entire shape of the arm. We then uniformly divided the length of the arm to 2-5 segments (from each time instance) and applied cubic spline technique to reconstruct the bending shape. To quantify the reconstruction quality, per time instance, we used the maximum Euclidean distance between the reconstructed curve and the actual shape. Figure 4 shows the error progression for discrete jointed systems having 2-5 rigid segments. It can be seen that 5-link system handles the deformation with less than 3 mm maximum error (and 1.3 mm mean error) for the duration of the experiment. Notice that low order discretizations could lead to large errors (spikes around 4.1 s) when the cubic spline method is applied.

Figure 5 shows some instances of this experiment where we compare the actual data (+ marks) and the reconstructed curve (solid line) along with the discrete points used for shape reconstruction. It can be seen that the shape reconstruction is identical without noticeable departure from the measured curve. Thus, we use a 5-link discrete approximation for the development of the dynamic model.

B. Kinematic Model

Figure 6-A shows the schematic of the planar 5-link discrete system model. Without losing generality, consider any i^{th} link of the discrete model which has l_i length. Note that, as we determine the discrete joins from the FOSS data points, the link lengths, though close, are not identical. We noted that this approach produces better fit when reconstructing the curve from discrete points. As shown in Fig. 1 the unactuated SBA has a noticeable curvature (see Fig. 1). Thus, each link has an angle offset θ_{i0} relative to the previous segment while θ_i is the joint-space variable. Note that, SBA system only has a single actuated DOF but, due to compliance, has infinitely many DOF. Our approach attempts to find a middle ground (with 5 DOF) to emulate the complete system with minimal error while enabling real-time dynamics. In addition, approximation of the SBA to a rigid-linked system facilitates the use of rigid-bodied dynamic algorithms that are numerically efficient and thus ideally suitable for real-time applications.

Utilizing standard homogeneous transformation techniques, we can derive the homogeneous transformation matrix (HTM) for the i^{th} segment, $\mathbf{T}_i \in \mathbb{SE}^2$ is given by (1) where $\mathbf{R}_z \in \mathbb{SO}^2$ models the rotation about the +Z axis and $\mathbf{P}_y \in \mathbb{R}$ is the translation along the +Y axis. $\mathbf{R}_i \in \mathbb{R}^{2\times2}$ and $\boldsymbol{p}_i \in \mathbb{R}^{2\times1}$ are the segment rotational and translation matrices with respect to the local coordinate system, $\{O_i\}$.

$$\mathbf{T}_i(\theta_i) = \mathbf{R}_{\mathbf{y}}(\theta_i + \theta_{i0})\,\mathbf{P}_z(l_i) = \begin{bmatrix} \mathbf{R}_i & \boldsymbol{p}_i \\ 0 & 1 \end{bmatrix} \tag{1}$$

By means of standard serial link kinematics, the HTM of the i^{th} link, $\mathbf{T}^i : \boldsymbol{q}_i \mapsto \mathbb{SE}^2$, in the task-space coordinates is given by (2) where $\boldsymbol{q}_i = [\theta_1 \cdots \theta_i]^T \in \mathbb{R}^i$ is the joint-space variable and $\mathbf{R}^i \in \mathbb{R}^{2\times 2}$ and $\boldsymbol{p}^i \in \mathbb{R}^{2\times 1}$ are the segment rotational and translation matrices with respect to$\{O\}$.

$$\mathbf{T}^i = \prod_{k=1}^{n} \mathbf{T}_k = \begin{bmatrix} \mathbf{R}^i & \boldsymbol{p}^i \\ 0 & 1 \end{bmatrix} \tag{2}$$

Based on (2), we can derive the recursive relationships for $\mathbf{R}^i$ and $\boldsymbol{p}^i$ as

$$\begin{aligned} \mathbf{R}^i &= \mathbf{R}^{i-1}\mathbf{R}_i \\ \boldsymbol{p}^i &= \boldsymbol{p}^{i-1} + \mathbf{R}^{i-1}\boldsymbol{p}_i \end{aligned} \tag{3}$$

where $\mathbf{R}^{i-1}$ and $\boldsymbol{p}^{i-1}$, according to our definition, is the tip coordinates of the prior, $(i-1)^{th}$ segment.

We take the time derivative of (3) to compute the body velocity (velocity with respect to coordinate frame at the center of gravity, shown in Fig. 6-B), of the i^{th} section in recursive form as

$$\begin{aligned} \boldsymbol{\Omega}_i &= \mathbf{R}_i^T\left(\boldsymbol{\Omega}_{i-1}\mathbf{R}_i + \dot{\mathbf{R}}_i\right) \\ \boldsymbol{\upsilon}_i &= \mathbf{R}_i^T\left(\boldsymbol{\upsilon}_{i-1} + \boldsymbol{\Omega}_{i-1}\boldsymbol{p}_i + \dot{\boldsymbol{p}}_i\right) \end{aligned} \tag{4}$$

where $\boldsymbol{\Omega}_i \in \mathbb{R}^{2\times 2}$ and $\boldsymbol{\upsilon}_i \in \mathbb{R}^{2\times 1}$ are the skew symmetric angular velocity matrix and linear velocity vector respectively [22]. The angular velocity, $\boldsymbol{\omega} \in \mathbb{R}$ can be derived from from $\boldsymbol{\Omega}_i$, as $\boldsymbol{\omega}_i = \boldsymbol{\Omega}_i^{\vee}$(see Tab. I for mathematical operator definitions).

Utilizing (4), the recursive linear body velocity Jacobian, $\mathbf{J}_i^{\upsilon} = \frac{\partial \boldsymbol{\upsilon}_i}{\partial \dot{\boldsymbol{q}}_i^T} \in \mathbb{R}^{2\times i}$, and angular body velocity Jacobian, $\mathbf{J}_i^{\Omega} = \frac{\partial \boldsymbol{\Omega}_i}{\partial \dot{\boldsymbol{q}}_i^T} \in \mathbb{R}^{2\times 2i}$ are given by

$$\begin{aligned} \mathbf{J}_i^{\Omega} &= \mathbf{R}_i^T\left[\ \mathbf{J}_{i-1}^{\Omega}\mathbf{R}_i \ \middle|\ \mathbf{R}_{i,\boldsymbol{q}_i}\ \right] \\ \mathbf{J}_i^{\upsilon} &= \mathbf{R}_i^T\left[\ \mathbf{J}_{i-1}^{\upsilon} + \mathbf{J}_{i-1}^{\Omega}\boldsymbol{p}_i \ \middle|\ \boldsymbol{p}_{i,\boldsymbol{q}_i^T}\ \right] \end{aligned} \tag{5}$$

Utilizing the Jacobians in (5), the angular velocity Hessian, $\mathbf{H}_i^{\Omega} = \frac{\partial \mathbf{J}_i^{\Omega}}{\partial \boldsymbol{q}_i} \in \mathbb{R}^{2i\times 2i}$ is derived in (6) and linear velocity Hessian, $\mathbf{H}_i^{\upsilon} = \frac{\partial \mathbf{J}_i^{\upsilon}}{\partial \boldsymbol{q}_i} \in \mathbb{R}^{2i\times i}$ is given by

$$\mathbf{H}_i^{\Omega} = \left[\begin{array}{c|c} \mathbf{R}_i^T\mathbf{H}_{i-1}^{\Omega}\mathbf{R}_i & \mathbf{0} \\ \hline \begin{array}{c}\mathbf{R}_{i,\boldsymbol{q}_i}^T\mathbf{J}_{i-1}^{\Omega}\mathbf{R}_i\cdots \\ +\mathbf{R}_i^T\mathbf{J}_{i-1}^{\Omega}\mathbf{R}_{i,\boldsymbol{q}_i}\end{array} & \begin{array}{c}\mathbf{R}_{i,\boldsymbol{q}_i}^T\mathbf{R}_{i,\boldsymbol{q}_i^T}\cdots \\ +\mathbf{R}_i^T\mathbf{R}_{i,\boldsymbol{q}_i^T,\boldsymbol{q}_i}\end{array} \end{array}\right] \tag{6}$$

$$\mathbf{H}_i^{\upsilon} = \left[\begin{array}{c|c} \mathbf{R}_i^T\left(\mathbf{H}_{i-1}^{\upsilon} + \mathbf{H}_{i-1}^{\Omega}\boldsymbol{p}_i\right) & 0 \\ \hline \begin{array}{c}\mathbf{R}_{i,\boldsymbol{q}_i}^T\left(\mathbf{J}_{i-1}^{\upsilon} + \mathbf{J}_{i-1}^{\Omega}\boldsymbol{p}_i\right)\cdots \\ +\mathbf{R}_i^T\mathbf{J}_{i-1}^{\Omega}\boldsymbol{p}_{i,\boldsymbol{q}_i}\end{array} & \begin{array}{c}\mathbf{R}_{i,\boldsymbol{q}_i}^T\boldsymbol{p}_{i,\boldsymbol{q}_i^T}\cdots \\ +\mathbf{R}_i^T\boldsymbol{p}_{i,\boldsymbol{q}_i^T,\boldsymbol{q}_i}\end{array} \end{array}\right] \tag{7}$$

These kinematic relationships will be used in the derivation of equations of motion (EoM) in the next section. For a detailed treatment of numerically efficient dynamic formulations, the readers are referred to [23].

C. Dynamic Model

In this section, we derive the EoM of the system, given by (8), recursively.

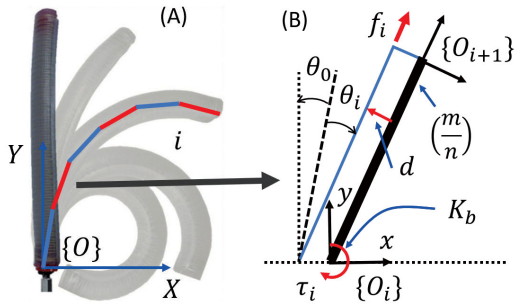

Fig. 6. Schematic of the discrete model. (Left) the discrete jointed reduced order model of SBA show in the task-space coordinate system, $\{O\}$, (Right) shows the segment variables relative to its body coordinate frame, $\{O_i\}$, related physical properties (further detailed in Section III-C).

$$\mathbf{M}\ddot{\boldsymbol{q}} + (\mathbf{C}+\mathbf{D})\,\dot{\boldsymbol{q}} + \boldsymbol{G} = \boldsymbol{\tau} \tag{8}$$

where $\mathbf{M}$, $\mathbf{C}$, $\mathbf{D}$, $\boldsymbol{G}$, and $\boldsymbol{\tau}$ are respectively the generalized inertia matrix, centrifugal and Coriolis force matrix, damping force matrix, conservative force matrix, and the joint-space torque applied to each link.

Prior work by the authors in [23] derives the relationship of individual links of serially arranged robots to the final EoM. For instance, the $\mathbf{M} = \sum \mathbf{M}_i$ with $\mathbf{M}_i$ being the generalized inertia matrix contribution from the i^{th} segment given by

$$\mathbf{M}_i = m_i\left(\mathbf{J}_i^{\upsilon}\right)^T\mathbf{J}_i^{\upsilon} + \left(\mathbf{J}_i^{\omega}\right)^T\mathcal{I}_{\omega}\mathbf{J}_i^{\omega} \tag{9}$$

where $\mathbf{J}_i^{\omega} = \left(\mathbf{J}_i^{\Omega}\right)^{\vee}$, $m_i = \frac{m}{5}$ is the mass of one segment. Considering the SBA as a semi-annular cylinder (shown in Fig. 2), the moment of inertia of a segment about the local coordinates is $\mathcal{I}_{\omega} = \frac{1}{3}m_i\frac{l_i^2}{25}$.

Similarly, $\mathbf{C} = \sum \mathbf{C}_i$ and $\mathbf{C}_i$ can be derived from Christoffell symbols of the second kind [22], which in turn utilizes the partial derivatives of $\mathbf{M}_i$, given by

$$\frac{\partial \mathbf{M}_i}{\partial q_h} = 2m_i\left(\mathbf{H}_i^{\upsilon}\right)_h^T\mathbf{J}_i^{\upsilon} + 2\left(\mathbf{H}_i^{\omega}\right)_h^T\mathcal{I}_{\omega}\mathbf{J}_i^{\omega} \tag{10}$$

where $\left(\mathbf{H}_i^{\upsilon}\right)_h = \mathbf{J}_{i,h}^{\upsilon}$ and $\left(\mathbf{H}_i^{\omega}\right)_h = \mathbf{J}_{i,h}^{\omega}$.

Following the same cumulative relationship, $\boldsymbol{G} = \sum \boldsymbol{G}_i$. The $\boldsymbol{G}_i$ is derived by assuming a torsional spring at each joint (this depicts the elastic property of the soft material used in the fabrication) as $\boldsymbol{G}_i$=$K_b\theta_i$ where K_b is the fictitious torsional spring coefficient at the joints.

Considering an semi-annular cross-section and the area mo-

TABLE I
NOMENCLATURE OF MATHEMATICAL OPERATORS

Operator	Definition
$(\ )_{,\boldsymbol{q}}$	Partial derivative with respect to elements of $\boldsymbol{q}$ along the dimension of $\boldsymbol{q}$. Eg. if $\boldsymbol{q} \in \mathbb{R}^{n\times 1}$ and $\mathbf{A} \in \mathbb{R}^{u\times v}$, then $\mathbf{A}_{,\boldsymbol{q}} \in \mathbb{R}^{nu\times v}$ and $\mathbf{A}_{,\boldsymbol{q}^T} \in \mathbb{R}^{u\times nv}$ respectively.
$(\ )^{\vee}$	Form the angular velocity vector of $\mathbb{R}$ from skew symmetric angular velocity matrix of $\mathbb{R}^{2\times 2}$. $(\ )^{\wedge}$ denotes the inverse operation.
$\mathbb{D}$	Form a diagonal matrix from the enclosed vector as the principal diagonal

ment of the shape, we can find the point of action to compute the external torque, $\tau_i = pAd$ where $d = \frac{4r_2}{3\pi}$ (d shown in Fig. 6-B), p is pressure, and $A = \frac{\pi r_2^2}{2}$ is the SBA cross-section area. K_b and $\mathbf{D}$ are computed via an experimental characterization process, similar to the approach reported in [23]. Therein, the SBA is supplied rectangular inputs and the response is recorded. The EoM were implemented in the Matlab computational environment (non-optimized) and run at 1.5 kHz. The model is solved using the Matlab Simulink platform using the ODE15s solver. Then, we define a cost-function which is based on the root mean square value of the difference between the experimental data and simulated output. Utilizing the Matlab global search framework with fmincon constrained optimization technique, the model is solved to find the optimal $K_b = 1.6067$ and $\mathbf{D} = 10^{-3}\mathbb{D}\left([8, 8, 8, 8, 8]\right)$ values.

IV. Experimental Validation

The EoM derived in III-C are then compared against the experimental data. Fig. 7 shows the step response comparison for a rectangular pressure signal of 119 kPa for 2.76 s starting at 0.12 s. The maximum bending associated with this experiment is shown in Fig. 8-1. The plot shows the X and Y coordinate trajectories of the 5 tip positions of the discrete dynamic model (numbered from 1-5). Empirical results suggest that the numerical model simulates the SBA well. The abrupt pressure increase causes the SBA to move suddenly causing the entire arm to oscillate. The oscillation of the experiments is due to the momentum and compliance of the SBA. Due to the friction of the system, the step response is under-damped with oscillation frequency about 5 Hz. Note that the SBA models proposed so far [13], [18] are yet to model this behavior at such high frequencies. The proposed model successfully simulates the SBA response well overall. Particularly, the model is able to model the under-damped oscillations along the length of the arm. We can observe some steady state errors towards the end of the simulation. This is due to the hysteresis inherent in SBAs. In this model, we have not considered the hysteresis, but this could be accounted for via an appropriate hysteresis model, such as the one reported by the authors in [15].

The next input signal is a rectangular pressure signal of 142 kPa starting and ending at 0.28 s and 2.36 s respectively. The maximum bending for this pressure input is shown in Fig. 8-2 and the position coordinate trajectories shown in Fig. 9. This causes the SBA to bend significantly more and, as a result, exhibits significant overshoot and takes longer to achieve steady state. Our model correctly simulates the overall behavior. Some steady state error can be observed in the X and Y coordinate points of the fifth segment with out of phase oscillation toward the end.

A third experiment also applies a rectangular pressure signal of 198 kPa amplitude which starts at 0.4 s and terminates at 2.04 s. This high pressure causes the arm to deform even more (as shown in Fig. 8-3) and the resulting coordinate trajectories are included in Fig. 10. As expected of an under-damped system, this step input causes the SBA to overshoot about

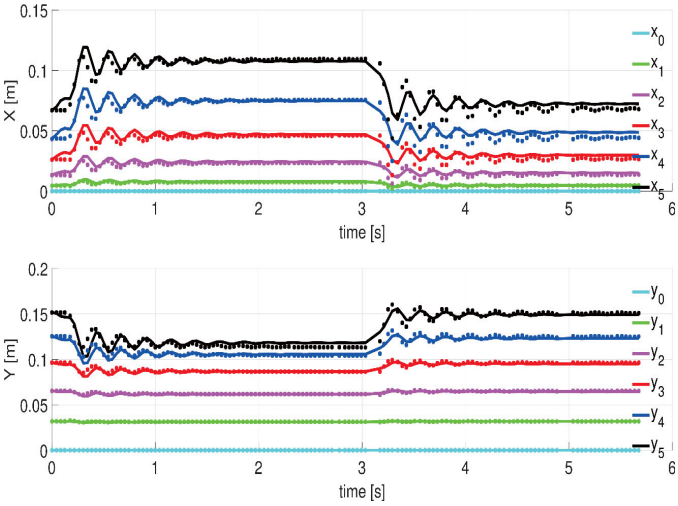

Fig. 7. Experiment one: Comparison of the simulated results against the experimental results. The subscripts of the X,Y coordinates denotes the task-space trajectories of the tips of segments relative to $\{O\}$.

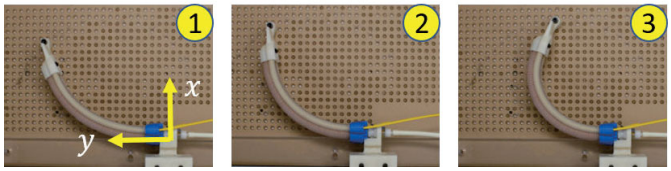

Fig. 8. Maximum bending of SBA related to Figs. 7 (Left), 9 (Center), and 10 (Right) from the neutral position shown in Fig. 1.

50% (see Y coordinates). The X-5 coordinate does not show much oscillation but this is due to its displacement at this pressure being parallel to Y axis (see Fig. 8-3) while the Y-5 and X-1 to X-4 trajectories capture the overshoot. Likewise, the system again shows oscillatory behavior when the pressure is removed and our model simulates this phenomenon correctly. To the best of our knowledge, this is the first time a SBA was subjected to a comprehensive dynamic analysis and lays the foundation to subsequent dynamic control of SBA-based soft and continuum robotic systems. The proposed numerically efficient dynamics could be utilized in real-time for implementing inverse dynamics control schemes involving both feedback and feed-forward techniques. In addition, this numerical framework could be used to model SBA systems for design optimization to meet desired mechanical and dynamic characteristics and applications in contact estimation and environmental sensing [19].

V. Conclusions

Soft bending actuators have strong potential for applications in non-structured and human-friendly robotic applications. To date, their potential has not been realized and the authors hypothesize that this is due to their lack of controllability which in turn depends on sophisticated feedback systems and advanced models. To address the former point, in this work, we integrate a SBA with FOSS sensor to obtain high fidelity

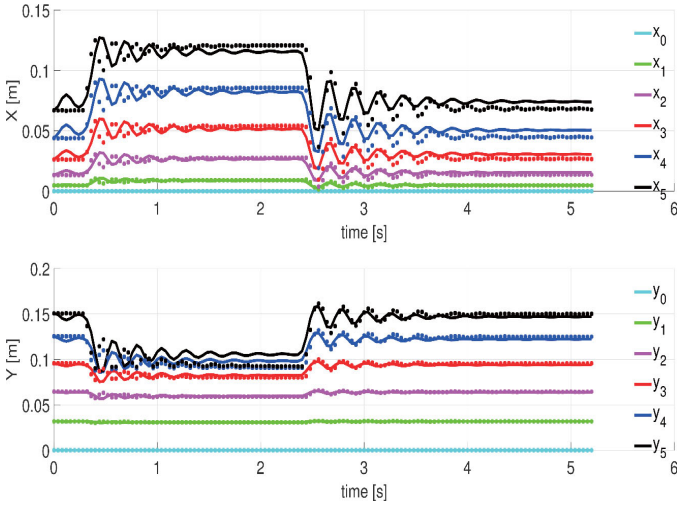

Fig. 9. Experiment two: Comparison of the simulated results against the experimental results. The subscripts of the X,Y coordinates denotes the task-space trajectories of the tips of segments relative to $\{O\}$.

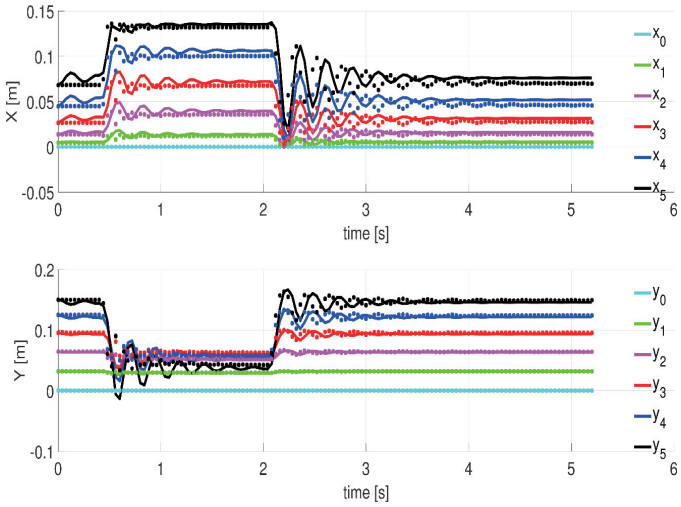

Fig. 10. Experiment three: Comparison of the simulated results against the experimental results. The subscripts of the X,Y coordinates denotes the task-space trajectories of the tips of segments relative to $\{O\}$.

data of the entire SBA structure at 75 Hz rate to achieve orders of magnitude better (than state of the art techniques) sensing of the SBA state-space. To effectively benefit from this data, we systematically identified and proposed a reduced-order dynamic model to facilitate real-time computations. The non-optimized Matlab implementation of the model, runs at 1.5 kHz (suitable for real-time computations), and was compared against the experimental data to validate the model. The proposed model showed good agreement and captures the dynamic behavior of SBA for different input signals. Based on this model, our future work will focus on implementing dynamic control and applications in environmental sensing.

REFERENCES

[1] I. S. Godage, R. Wirz, I. D. Walker, and R. J. Webster, "Efficient spatial dynamics for continuum arms," in *ASME 2015 Dynamic Systems and Control Conference*. American Society of Mechanical Engineers, 2015, pp. V003T53A005–V003T53A005.

[2] H. Lipson, "Challenges and opportunities for design, simulation, and fabrication of soft robots," *Soft Robotics*, vol. 1, no. 1, pp. 21–27, 2014.

[3] R. J. Webster III and B. A. Jones, "Design and kinematic modeling of constant curvature continuum robots: A review," *The International Journal of Robotics Research*, vol. 29, no. 13, pp. 1661–1683, 2010.

[4] I. S. Godage, R. Wirz, I. D. Walker, and R. J. Webster III, "Accurate and efficient dynamics for variable-length continuum arms: a center of gravity approach," *Soft Robotics*, vol. 2, no. 3, pp. 96–106, 2015.

[5] D. Trivedi, C. D. Rahn, W. M. Kier, and I. D. Walker, "Soft robotics: Biological inspiration, state of the art, and future research," *Applied bionics and biomechanics*, vol. 5, no. 3, pp. 99–117, 2008.

[6] C. Majidi, "Soft robotics: a perspective - current trends and prospects for the future," *Soft Robotics*, vol. 1, no. 1, pp. 5–11, 2014.

[7] I. S. Godage, T. Nanayakkara, and D. G. Caldwell, "Locomotion with continuum limbs," in *Intelligent Robots and Systems (IROS), 2012 IEEE/RSJ International Conference on*. IEEE, 2012, pp. 293–298.

[8] T. Zheng, I. S. Godage, D. T. Branson, R. Kang, E. Guglielmino, G. A. Medrano-Cerda, and D. G. Caldwell, "Octopus inspired walking robot: design, control and experimental validation," in *Robotics and automation (ICRA), 2013 IEEE international conference on*, 2013, pp. 816–821.

[9] K. C. Galloway, K. P. Becker, B. Phillips, J. Kirby, S. Licht, D. Tchernov, R. J. Wood, and D. F. Gruber, "Soft robotic grippers for biological sampling on deep reefs," *Soft Robotics*, vol. 3, no. 1, pp. 23–33, 2016, pMID: 27625917. [Online]. Available: https://doi.org/10.1089/soro.2015.0019

[10] J. Burgner-Kahrs, D. C. Rucker, and H. Choset, "Continuum robots for medical applications: A survey," *IEEE Transactions on Robotics*, vol. 31, no. 6, pp. 1261–1280, 2015.

[11] R. F. Shepherd, F. Ilievski, W. Choi, S. A. Morin, A. A. Stokes, A. D. Mazzeo, X. Chen, M. Wang, and G. M. Whitesides, "Multigait soft robot," *Proceedings of the national academy of sciences*, vol. 108, no. 51, pp. 20 400–20 403, 2011.

[12] S. Kim, C. Laschi, and B. Trimmer, "Soft robotics: a bioinspired evolution in robotics," *Trends in biotechnology*, vol. 31, no. 5, pp. 287–294, 2013.

[13] P. Polygerinos, Z. Wang, J. T. Overvelde, K. C. Galloway, R. J. Wood, K. Bertoldi, and C. J. Walsh, "Modeling of soft fiber-reinforced bending actuators," *IEEE Trans. on Robotics*, vol. 31, no. 3, pp. 778–789, 2015.

[14] F. Renda, M. Giorelli, M. Calisti, M. Cianchetti, and C. Laschi, "Dynamic model of a multibending soft robot arm driven by cables," *IEEE Transactions on Robotics*, vol. 30, no. 5, pp. 1109–1122, 2014.

[15] I. S. Godage, D. T. Branson, E. Guglielmino, and D. G. Caldwell, "Pneumatic muscle actuated continuum arms: Modelling and experimental assessment," in *Robotics and Automation (ICRA), 2012 IEEE International Conference on*. IEEE, 2012, pp. 4980–4985.

[16] I. S. Godage and I. D. Walker, "Dual quaternion based modal kinematics for multisection continuum arms," in *Robotics and Automation (ICRA), 2015 IEEE International Conference on*. IEEE, 2015, pp. 1416–1422.

[17] I. S. Godage, G. A. Medrano-Cerda, D. T. Branson, E. Guglielmino, and D. G. Caldwell, "Modal kinematics for multisection continuum arms," *Bioinspiration & biomimetics*, vol. 10, no. 3, p. 035002, 2015.

[18] P. Polygerinos, Z. Wang, K. C. Galloway, R. J. Wood, and C. J. Walsh, "Soft robotic glove for combined assistance and at-home rehabilitation," *Robotics and Autonomous Systems*, vol. 73, pp. 135–143, 2015.

[19] K. Galloway, Y. Chen, E. Templeton, B. Rife, I. Godage, and E. Barth, "Fiber optic shape sensing with a soft actuator for state estimation and planar environmental mapping," *Soft Robotics*, 2018 (under review).

[20] B. J. Soller, D. K. Gifford, M. S. Wolfe, and M. E. Froggatt, "High resolution optical frequency domain reflectometry for characterization of components and assemblies," *Optics Express*, vol. 13, no. 2, pp. 666–674, 2005.

[21] S. T. Kreger, N. A. A. Rahim, N. Garg, S. M. Klute, D. R. Metrey, N. Beaty, J. W. Jeans, and R. Gamber, "Optical frequency domain reflectometry: principles and applications in fiber optic sensing," in *Fiber Optic Sensors and Applications XIII*, vol. 9852. International Society for Optics and Photonics, 2016, p. 98520T.

[22] R. M. Murray, *A mathematical introduction to robotic manipulation*. CRC press, 2017.

[23] I. S. Godage, G. A. Medrano-Cerda, D. T. Branson, E. Guglielmino, and D. G. Caldwell, "Dynamics for variable length multisection continuum arms," *The International Journal of Robotics Research*, vol. 35, no. 6, pp. 695–722, 2016.